Title

High resolution three-dimensional reconstruction of the collagenous matrix of the human optic nerve head

Journal

Brain Research Bulletin, 81(2-3)

ISSN

03619230

Authors

Winkler, Moritz
Jester, Bryan
Nien-Shy, Chyong
et al.

Publication Date

2010-02-15

DOI

10.1016/j.brainresbull.2009.06.001

Peer reviewed

Brain Research Bulletin 81 (2010) 339–348

Contents lists available at ScienceDirect

Brain Research Bulletin

journal homepage: www.elsevier.com/locate/brainresbull

Research report

High resolution three-dimensional reconstruction of the collagenous matrix of the human optic nerve head

Moritz Winkler[1], Bryan Jester[1], Chyong Nien-Shy[1], Salina Massei[1], Don S. Minckler[1], James V. Jester[1], Donald J. Brown*

The Gavin Herbert Eye Institute, University of California, Irvine, 101 The City Drive, Orange, CA 92868, United States

ARTICLE INFO

Article history:
Received 13 March 2009
Received in revised form 29 May 2009
Accepted 4 June 2009
Available online 11 June 2009

Keywords:
Glaucoma
Lamina cribrosa
Collagen
Extracellular matrix
Anatomy

ABSTRACT

Glaucoma is the second most common cause of blindness worldwide, leading to irreversible loss of vision. Prior studies indicate that ocular pressure-induced displacement of the lamina cribrosa (LC) may be responsible for retinal ganglion cell axon damage inside the neural canal. We present a novel approach to imaging the entire lamina cribrosa and the scleral canal at high lateral and axial resolution by using a combination of array tomography and nonlinear optical imaging of serial ultrathin orthogonal sections to detect second harmonic generated (SHG) signals from collagen. The resulting images can be analyzed individually or combined to form a three-dimensional reconstruction of the lamina. Due to the specificity of SHG generated from collagen the density and distribution of collagen inside the scleral canal can be objectively quantified with a high degree of accuracy. The reconstruction shows a non-uniform distribution of collagen along both the longitudinal and orthogonal axes. Mapping the collagen density by geographic region reveals significant differences in collagen content that result in "thin spots" with low collagen density as well as areas of very high collagen content. This suggests a non-uniform mechanical stiffness across the lamina that may account for increased axon damage observed in glaucoma patients. The inferior temporal region of the ONH in particular is marked by low collagen density, which corresponds with clinical observations identifying this region as being more susceptible to damage during the onset of glaucoma. Further application of this technique will help characterize the relationship of age, race and gender on the morphology of the LC.

1. Introduction

Glaucoma accounts for over 12% of global blindness [28], representing a serious health problem especially considering the irreversibility of glaucoma-induced optic nerve damage. Approximately 50% of glaucoma cases are of the primary open angle (POAG) variant. Clinically, POAG is described as a progressive visual field loss [8,9] and posterior displacement of the lamina cribrosa (LC), cupping of the optic nerve head (ONH), thinning of prelaminar tissue with axonal dropout in the ONH, and death of retinal ganglion cells (RGC) [27,22].

Past studies have observed that increased intraocular pressure (IOP), a major risk factor for glaucomatous change, results in blocking of retrograde and anterograde axonal transport [19] as well as dilation of axons passing through the ONH precisely at the level of the lamina cribrosa (LC). The LC is a sieve-like structure inside the scleral canal comprised of overlapping and branching collagenous beams [16]. These collagen beams form pores through which retinal ganglion cell axons transit to exit the eye. Generally, it is thought that the lamina cribrosa provides structural support to the exiting axons and the vascular supply of the ONH, while helping maintain the pressure differential between the inner eye and the central nervous system. This has led to the theory that an increase in intraocular pressure (IOP) causes pores to deform as the lamina is displaced posteriorly [31], exerting additional stress on the axons and blood vessels which can initiate nerve cell death and subsequent loss of vision. As the primary load-bearing tissue in the scleral canal, the lamina cribrosa has therefore been thought to play a major role in the development of glaucoma [25,14]. To better understand these factors and to model the underlying processes, it is necessary to study the entire structure of the lamina cribrosa at high resolution.

Numerous studies have examined the structure of the LC using both optical [2,32,20,13] and electron microscopy [12,10,29]. Burgoyne et al. recently presented a method to reconstruct the primate

* Corresponding author at: University of California, Irvine, Ophthalmology Research, Irvine, CA 92697-4380, United States. Tel.: +1 714 456 7368.
E-mail addresses: moritzw@uci.edu (M. Winkler), bjester@uci.edu (B. Jester), cnienshy@uci.edu (C. Nien-Shy), smassei@uci.edu (S. Massei), minckler@hs.uci.edu (D.S. Minckler), jjester@uci.edu (J.V. Jester), dbrown@uci.edu (D.J. Brown).
[1] Address: University of California, Irvine, Ophthalmology Research, Irvine, CA 92697-4380, United States.

0361-9230/$ – see front matter © 2009 Elsevier Inc. All rights reserved.
doi:10.1016/j.brainresbull.2009.06.001

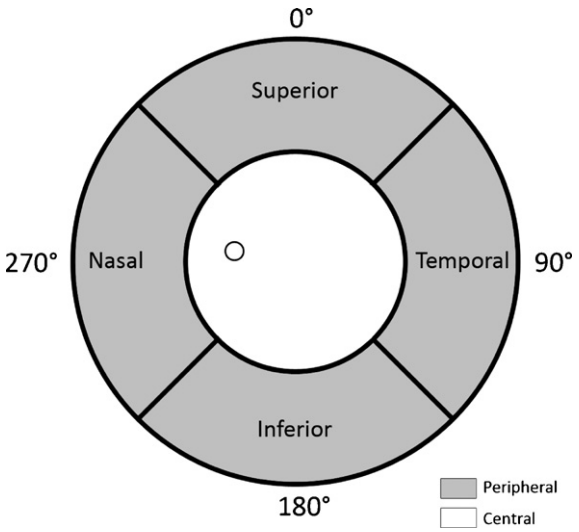

Fig. 1. Schematic drawing of an ONH cross-section. To analyze the distribution of collagen the ONH was divided into four peripheral sectors corresponding to anatomical quadrants. A detailed analysis for collagen content was performed by analyzing the average intensity along lines in 1° increments, starting with 0° at the 12 o'clock position.

LC using digital photography [6]. However, when examining the lamina cribrosa with traditional microscopic methods, researchers are faced with well-known problems caused by the inverse relationship between magnification and field of view (FoV). The high magnification required to resolve details of the substructure is associated with a very limited FoV, reducing the scope of the investigation and forcing researchers to focus their attention on one or several comparatively small regions of interest (ROI) that are geographically separated. While the collagen beams that make up the lamina have a diameter of a few microns, they form a larger meshwork with beam lengths and pore diameters several orders of magnitude larger than individual collagen fibers, extending far outside the FoV. Conversely, when reducing the magnification to extend the FoV to encompass the entire LC, details of the substructure such as individual beams can no longer be resolved. This "resolution gap" is an inherent problem of structural microscopy. To fully understand the biomechanical properties of the lamina cribrosa and to accurately quantify and ultimately model these properties, it is necessary to reconstruct the entire structure at high resolution to have sufficient data to understand the relationship between the finer elements that make up the tissue. Bridging the resolution gap between these scales can be achieved by acquiring multiple consecutive overlapping images and digitally combining them into a two-dimensional mosaic. A three-dimensional reconstruction can be obtained by combining 2D mosaics acquired at various depths throughout the tissue.

In recent years, nonlinear optical microscopy methods, particularly second harmonic generation (SHG) imaging, have improved to the point where they provide resolutions approaching the boundaries imposed by Abbe's diffraction limit, which specifies the maximum achievable resolution for any given optical system [1,2]. These developments have made highly detailed investigations of the LC possible [5]. Additionally, the ever increasing speed of personal computers has resulted in the widespread availability of inexpensive computing resources approaching performance levels commonly associated with supercomputers only a decade ago [11], enabling researchers to not only handle very large datasets but to also reconstruct and visualize them in 3D [3,30]. The ability to obtain high-resolution images and to process large datasets in the multiple-gigabyte range are necessary prerequisites to close the gap between scales.

In this report, we combined the high lateral resolution provided by multiphoton microscopy, the high axial resolution gained through array tomography [17], semi-automated image acquisition, and advanced data processing to bridge the resolution gap and image the LC at very high resolution. We applied this method to a human donor eye from a 53-year-old Hispanic male. Analyzing the resulting images for relative collagen content revealed a

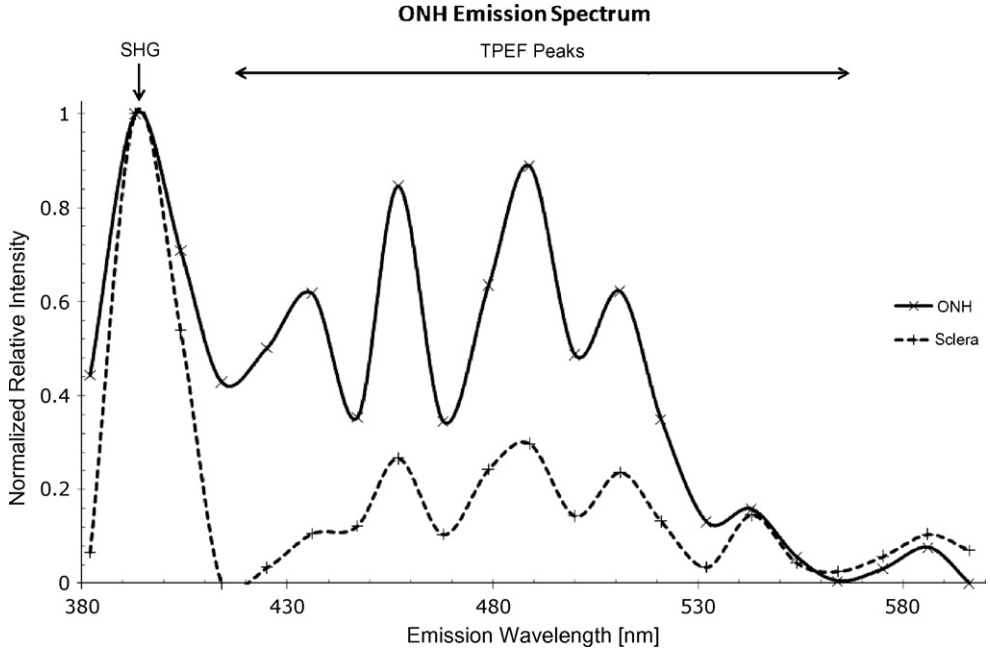

Fig. 2. Emission spectra of the sclera and a plastic section of human ONH tissue. The solid line shows the emissions generated from the ONH using an excitation frequency of 800 nm. The arrow marks the second harmonic peak at 400 nm. Secondary peaks at higher wavelengths indicate the presence of two photon excited fluorescence from other ONH components. Two-photon emissions from the sclera are indicated by the dashed line. Note the higher relative intensity of the SHG peak relative to the TPEF peaks. Secondary peaks match those of the ONH spectrum, suggesting a similar makeup.

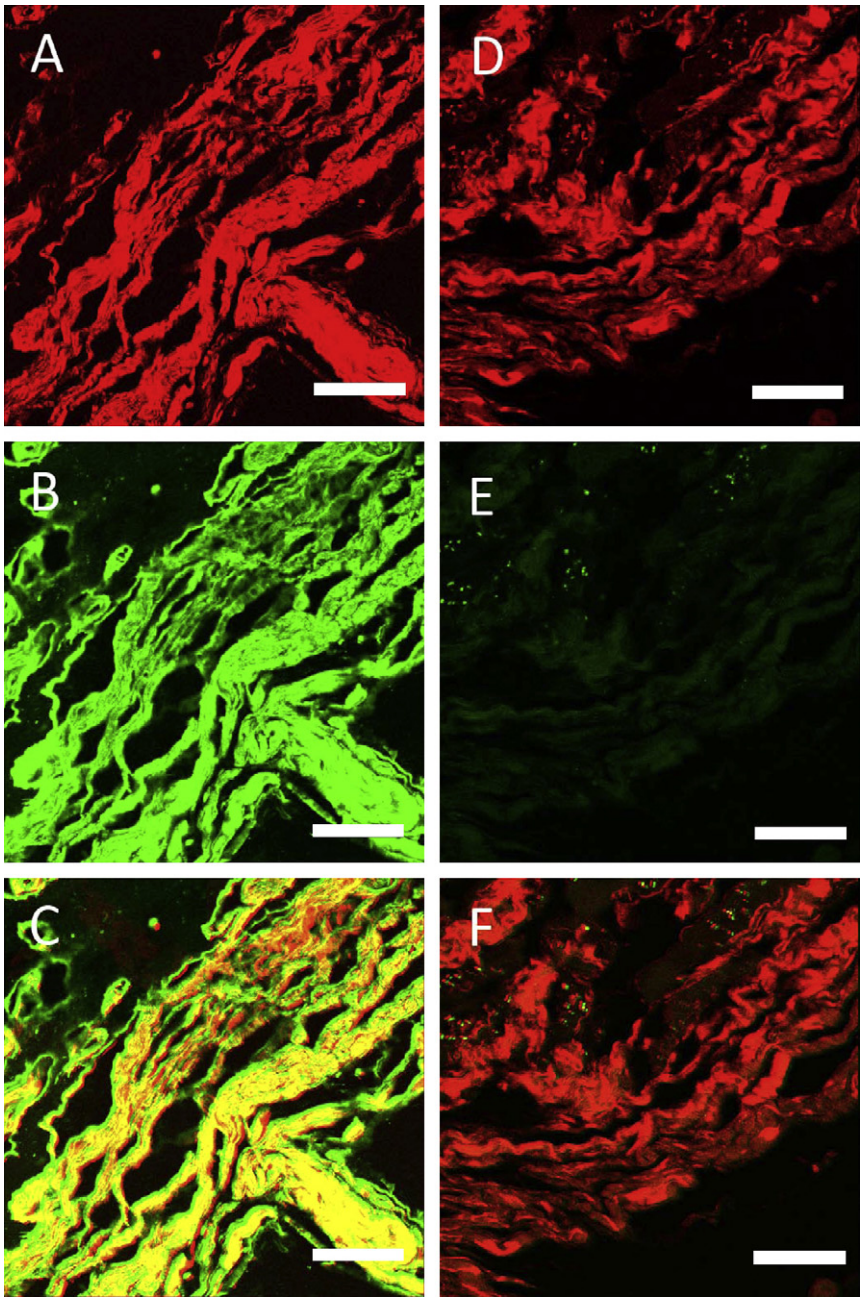

Fig. 3. Correlation of SHG and collagen immunostaining. Left panel: SHG image of human ONH tissue (A). The same area stained with an anti-collagen IgG antibody followed by secondary antibody (B). The overlay (C) confirms the colocalization. Right panel: SHG image of human ONH tissue (D), the same area stained with secondary antibody alone (E) and the resulting overlay (F). Bars: 100 μm.

non-homogenous distribution of collagen inside the scleral canal. The inferior aspect of the LC contained significantly fewer collagen beams, whereas a dense bundle of beams ran across the diameter of the LC in the nasal temporal direction. The high resolution images obtained by this method allowed for a precise quantification of relative collagen content in all three dimensions.

2. Materials and methods

2.1. Tissues

For the array tomography, autopsy eyes from a 53-year-old male Hispanic donor were obtained from the San Diego Eye Bank following institutional review board approval and following the tenets established by the Declaration of Helsinki. The globe was inspected under a stereo-microscope to assess the quality of the eye and to ensure the absence of any major visible defects or abnormalities in the retina and ONH. ONH tissue from the second eye was used for immunohistochemistry.

2.2. Immunohistochemistry

Human optic nerve head tissue fixed in formaldehyde was frozen in OCT (Sakura Finetec Inc., Torrance, CA). Sections (10 μm) in the coronal and sagittal plane were cut using a Leica CM1850 Cryotome (Leica, Wetzlar, Germany). Sections were air-dried, fixed in acetone at −20 °C, and rehydrated in phosphate buffered saline (PBS, pH 7.4). Sections were then blocked using goat serum (MP Biomedicals, Solon, OH) (1:10 in PBS) for 30 min followed by incubation for 1 h with mouse monoclonal type I anti-collagen in PBS (1:100, Abcam, Cambridge, MA). After washing with PBS, sections were reacted with FITC-conjugated goat anti-mouse IgG (Invitrogen, Carlsbad, CA) for 1 h, washed and mounted in glycerol/PBS (1:3). All incubations were carried out at 37 °C in a humidified chamber. A negative control was performed by omitting the primary antibody. ONH sections were then evaluated and imaged using a Zeiss LSM 510 microscope (Carl Zeiss MicroImaging Inc., Thornwood, NY).

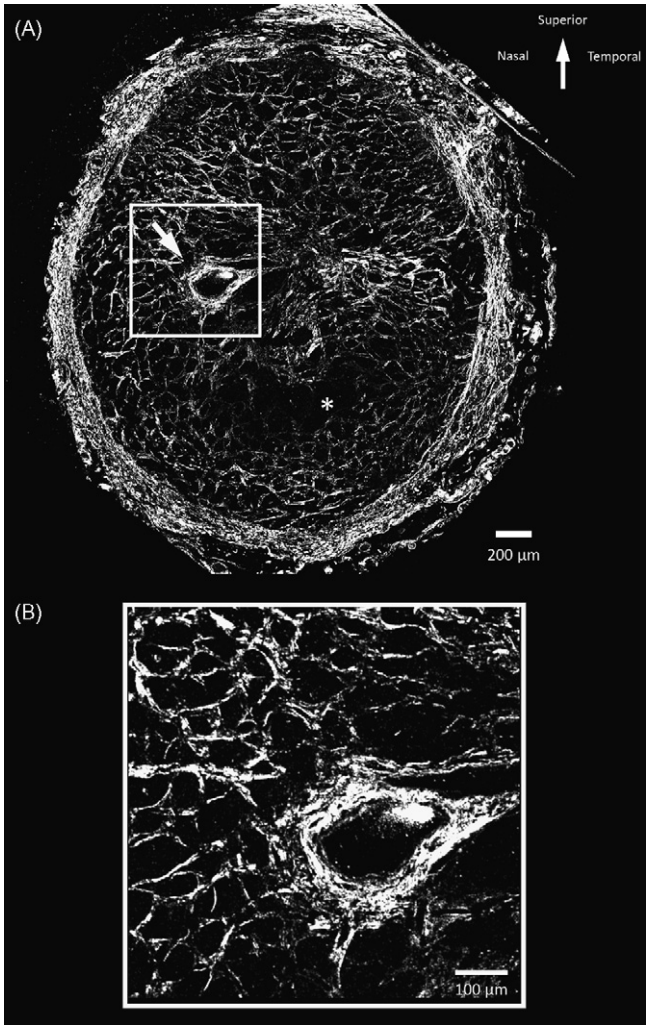

Fig. 4. Orthogonal cross-section of the lamina cribrosa obtained using SHG imaging. (A) A single plane image mosaic consisting of 49 individual image files scanned in sequence using an excitation wavelength of 800 nm. This image represents a physical section with a thickness of 2 μm. Native resolution for this image is 3584 × 3584 pixels. The arrow marks the location of the central artery. The laminar meshwork is clearly visible. (B) Magnified view of the area around the central artery. Owing to the high resolution, details such as the insertion of individual collagen beams into the central artery are clearly visible.

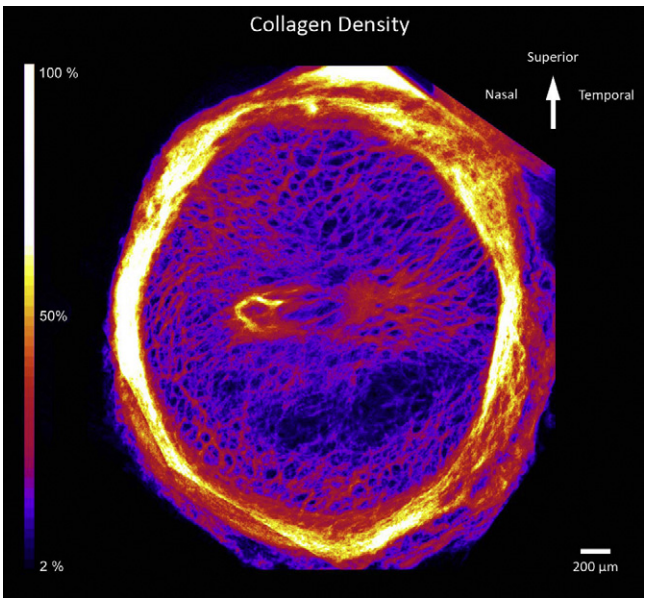

Fig. 5. Collagen density map of the ONH. To generate this image, an average z projection was performed on the image stack which was thresholded for collagen. A density of 100% indicates the presence of collagen in every plane of the stack, whereas a density of 0% corresponds to a complete lack of collagen in that particular location.

2.3. Array tomography

2.3.1. Embedding

The optic nerve head was dissected from the globe as a 5 mm × 5 mm block of tissue. The ONH was then fixed in 4% paraformaldehyde/PBS overnight at 4 °C. Afterwards the tissue was rinsed with 3.5% sucrose in PBS for 20 min three times followed by dehydration with graded series of ethanol, 30 min each. The sample was then immersed in LR White resin (Electron Microscopy Sciences, Hatfield, PA) three times for 30 min each, followed by an overnight immersion in LR White resin at 4 °C. The sample was then embedded in gelatin capsules and polymerized at 60 °C for 48 h.

2.3.2. Sectioning

The embedded sample was serially sectioned using 2 μm steps on a Leica Reichert Ultracut R Ultramicrotome (Leica Microsystems GmbH, Wetzlar, Germany). To produce ribbons of serial sections, Pattex Kraftkleber compact fast-drying glue (Henkel, Düsseldorf, Germany) was applied to the top and bottom of the block. Ribbons of sections were floated onto glass slides (Fisher Scientific Ltd, Houston, TX) coated with 0.1% gelatin and 0.01% chromium potassium sulfate and then dried on a slide warmer at 50 °C for 15 min. Each slide contained two ribbons of approximately 10 sections each. By maintaining the precise arrangement and orientation of slides in an anterior to posterior direction, this protocol created an array of ordered sections.

2.3.3. Imaging

Images were acquired with a Zeiss 510 Meta laser scanning microscope (Carl Zeiss MicroImaging Inc., Thornwood, NY) in multiphoton mode. To generate the multiphoton effects, ultrashort laser pulses from a Titanium: Sapphire femtosecond laser (Chameleon®, Coherent Inc., Santa Clara, CA) were used. The Ti:Sa laser offers tunable emission wavelengths between 730 and 940 nm. Tests revealed that changing the excitation wavelength yields different relative signal strengths for various tissue components such as collagen or elastin.

The sample was scanned with an excitation wavelength of 800 nm, which provided a strong SHG peak for collagen. The microscope is capable of acquiring several different wavelengths simultaneously, however for the purposes of this study only the backscatter SHG was collected using a (400 ± 10) nm band-pass filter. Each section was centered manually under the microscope and focused. All samples were scanned using a 20×/0.75 NA Zeiss Apochromat objective at a resolution of 512 by 512 pixels per image resulting in a lateral resolution of 0.91 μm per pixel. To counteract noise, each line was scanned twice and averaged. A total of 49 single-plane images arranged in a quadratic grid were acquired for each tissue section using the automated stage positioning feature. A 10% overlap between adjacent images resulted in a final resolution of 3584 × 3584 pixels per section and covered an area of 10.6 mm^2. The 49 tiles from each slice were concatenated using the Zeiss LSM microscope software and saved in Zeiss' native .LSM format as 8-bit multichannel image files.

2.4. Digital image analysis

2.4.1. Data export and post-processing

Due to the high pixel resolution of each section, the full image stack file size was just under 2 GB, necessitating the use of a high-end computer system. All image processing tasks were carried out on a PC with dual Intel Xeon Quad Core CPUs clocked at 2.5 GHz per core with 16 GB of RAM. To provide sufficient resources for visualizing the three-dimensional reconstructions, the computer was equipped with a Nvidia GeForce 270 graphics adapter with a full gigabyte of texture memory. The system was running the 64 bit version of Windows XP Professional SP2.

To facilitate easier data processing, the channels were separated by exporting each .LSM file as single-channel 8 bit TIFF image. This was achieved using the LSM Toolbox plugin for ImageJ version 1.39, which offers batch processing for large numbers of files. ImageJ is a free Java-based image processing platform developed by the National Institute of Health (http://rsb.info.nih.gov/ij/).

Single-channel images were batch-processed in Adobe Photoshop CS 2 (Adobe Systems Inc., San Jose, CA). To reduce noise, a median filter with a 2 pixel radius was applied. Following smoothing, the individual images were contrast-adjusted using Photoshop's Auto Contrast feature to further separate the signal from the background levels. The images were then combined in ImageJ to a single z-stack of 294 planes representing a tissue volume of 3.26 mm × 3.26 mm × 0.59 mm.

Unlike optical sections, the slices were not perfectly aligned as the individual plastic sections tended to rotate and translate relative to each other when floated onto the glass slides. To compensate for this, the planes were digitally realigned.

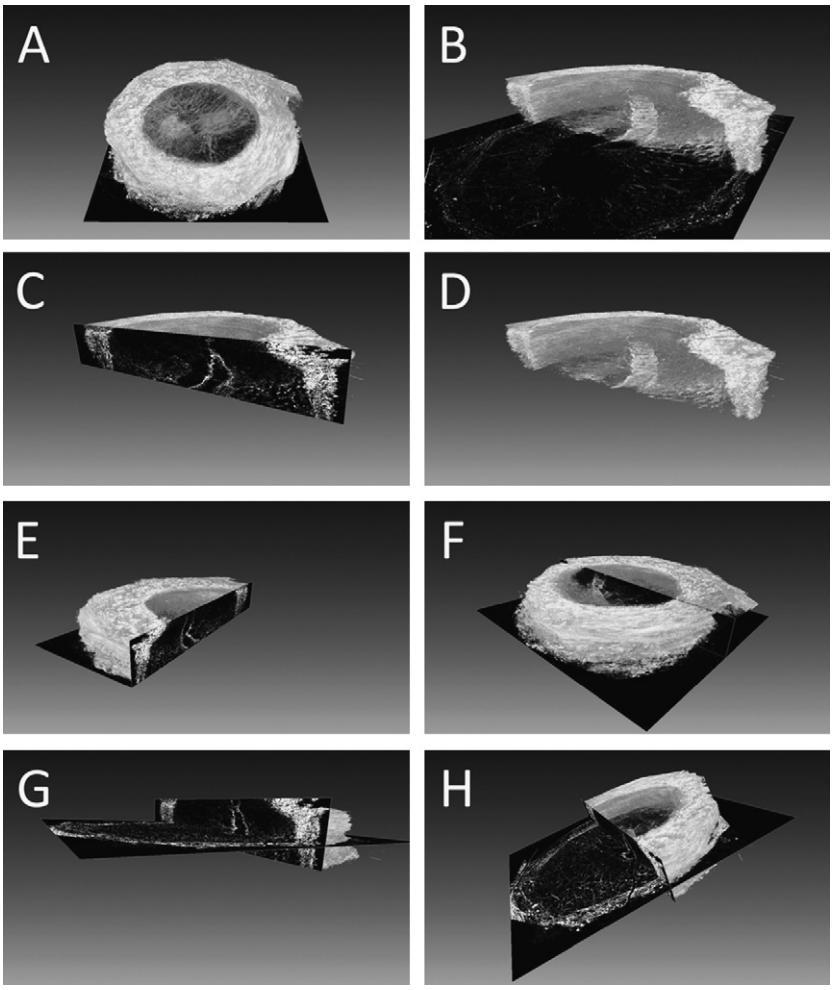

Fig. 6. Screenshots showing various 3D reconstructions of the ONH. An isometric view of the LC (A) shows the heterogeneous distribution of collagen inside the scleral canal. Longitudinal cuts (B)–(E) show the central artery. Both orthogonal and longitudinal cuts can be generated individually or simultaneously to assess the morphometry of the LC in all three dimensions (F)–(H).

Several tests demonstrated that automated registration algorithms such as ImageJ's StackReg plugin do not yield satisfactory results, and are ultimately inferior to manual alignments carried out by human operators. In addition, the automated registration required considerable amounts of RAM, a problem which was compounded by the large size of the image stacks. We therefore opted for manual alignment of slices using the AlignSlice module in Amira 5.2 (Visage Imaging, Carlsbad, CA) to compensate for the rotation and translation of individual image planes.

2.4.2. Image analysis and visualization

The fully aligned image stacks were loaded into MetaMorph 7.5 (Molecular Devices, Sunnyvale, CA) to perform morphometric analyses. For each section, the border between laminar tissue and the sclera canal wall was manually delineated. Due to the non-uniform makeup of the canal area, automated edge detection algorithms yielded poor recognition of the edges and required manual correction for the vast majority of images. Therefore, human operators were utilized to delineate the border. To exclude human bias, the manual delineation procedure was repeated several times by different operators. Each operator was instructed to draw a line along the perceived interface between scleral canal and lamina cribrosa. The deviation between operators when expressed as percent deviation from the mean value was calculated for each image. The average operator error was 1.75% per image.

Owing to the unique effect of SHG occurring only in structures lacking centrosymmetry, non-collagenous structures were not visible in the SHG channels. The images were thresholded to exclude pixel noise and binarized, with white pixels indicating the presence of structure. The threshold setting was based on maintaining an acceptable signal-to-noise ratio without distorting the density values. Given the a priori knowledge about the general structure of the LC, it was possible to set a realistic threshold value by comparing the amount of visible structure to the amount of noise at any given setting.

To calculate structure densities and pore sizes, the ratio of white to black pixels within a manually defined region was obtained through MetaMorph. This was performed on a per-image basis resulting in 294 data points, one for each image. Besides quantifying the total collagen volume within the entire scleral canal, the volume within defined regions of the canal area was measured. Four main central and peripheral quadrants were defined as shown in Fig. 1.

3. Results

The emission spectrum of the ONH is characterized by several distinct emission peaks (Fig. 2). The strongest peak is at $\lambda_{SHG} = \lambda_e/2$, where λ_e is the excitation wavelength. This first peak (arrow) marks the emission of second harmonic generated light. SHG emission from biological tissues is indicative of the presence of collagen, because its fibrillar structure satisfies the phase-matching condition required for the emission of second harmonic generated signals. Secondary peaks with $\lambda < \lambda_e$ indicate the presence of two photon excited fluorescence of various components of the ONH. In the sclera, the relative intensities of the TPEF peaks are markedly lower than those of the SHG peaks. This is likely due to a comparatively higher collagen density and/or a reduction in the fluorescent components in the sclera compared to the ONH.

As shown in Fig. 3, the immunostaining of the ONH tissue, utilizing a monoclonal antibody to type I collagen closely matched the results obtained from imaging the SHG signal. The same tissue features are visible in both the SHG channel (Fig. 3A) and the immunostained channel (Fig. 3B). The overlay (Fig. 3C) confirms the high degree of correlation between the two signals, confirming the correlation between collagen and the emission of second harmonic generated signals.

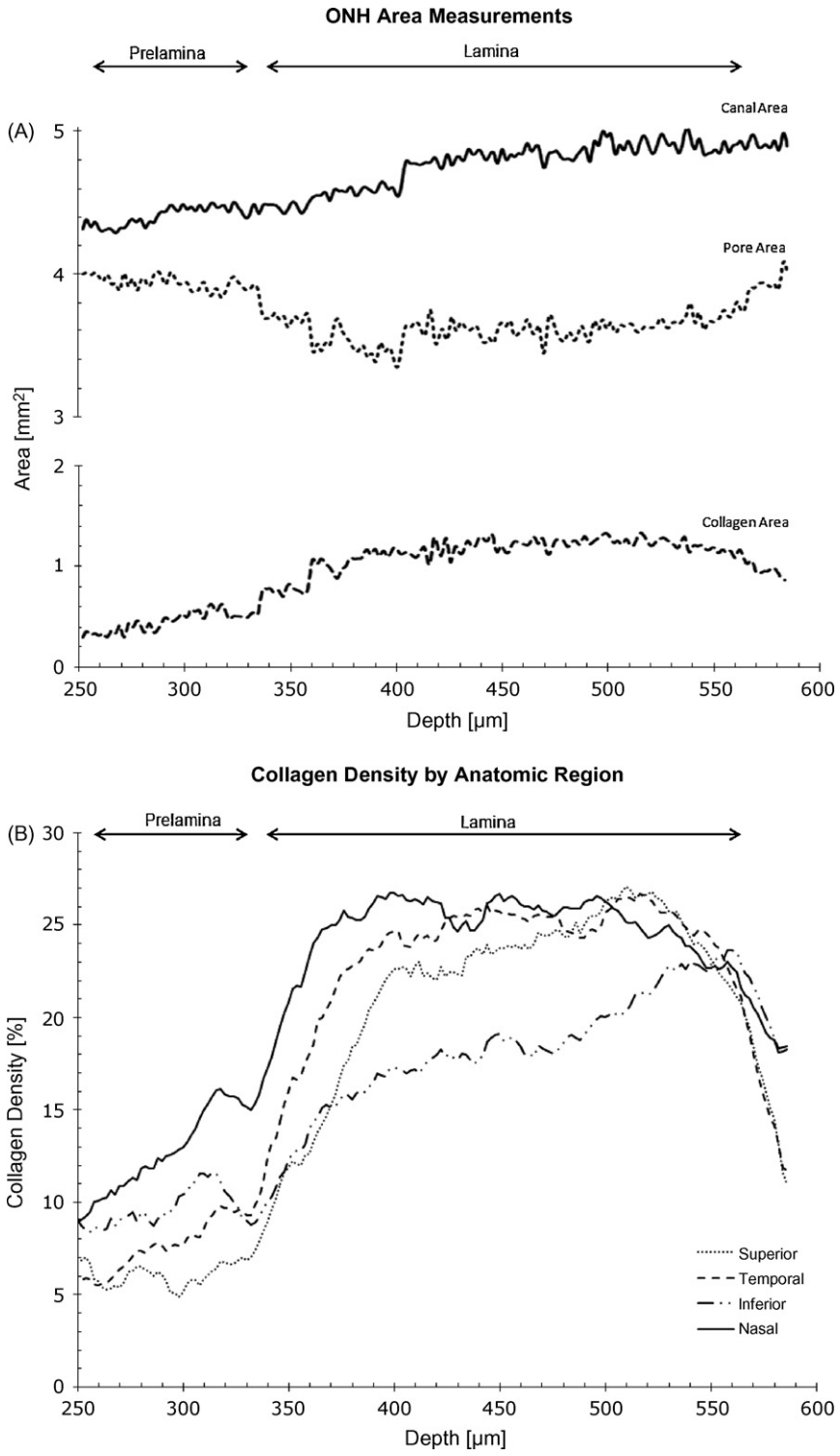

Fig. 7. ONH area and collagen density analysis. (A) Canal area, collagen area and total pore area throughout the ONH. The amount of available pore space is reduced inside the LC. (B) Collagen content per anatomical region plotted as a function of depth. Each plane was analyzed individually. The density increases significantly inside the LC.

To fully reconstruct the ONH in three dimensions, a block of tissue was embedded in plastic resin and serially sectioned. Each microtome section was scanned individually using a grid of 7×7 individual images. A correlation algorithm that is part of the Zeiss LSM software automatically corrected minor misalignments during the automated concatenation process. The resulting image (Fig. 4A) represents the 0.91 micron/pixel resolution while at the same time providing a field of view large enough to encompass the entire width of the ONH. This image shows a single 2 micron section from the laminar area. The scleral canal wall, with its high collagen content is visible as a ring-like structure surrounding the laminar meshwork. Due to the high resolution of these images, individual collagen beams are clearly distinguishable, as seen in Fig. 4B which shows a magnified view of the area around the central artery, which is marked by an arrow in Fig. 4A. These beams insert peripherally into the scleral canal wall and centrally into the central artery. The

inferior temporal region appeared to be deficient in collagen beams (asterisk) in most slides, suggesting a low collagen density in this region.

The slide shown in Fig. 4 demonstrates a variation in local collagen content but represents only a single 2 micron plane of the full dataset. To visualize the overall collagen distribution throughout the whole scanned volume, the image stack was thresholded and collapsed onto a single plane by performing an "average z" projection. The resulting average gray values were mapped to a full-color lookup table to better visualize the variability in density within the dataset. Fig. 5 shows the resulting image which represents a full-resolution density map of the collagen distribution throughout the ONH. In this image, cooler colors correspond to lower average collagen content as indicated by the scaling bar. Black pixels indicate the absence of collagen throughout the entire stack in that particular location. Cooler colors represent a low collagen density, whereas hot colors indicate a high collagen content throughout the stack. In this image, the scleral ring and the central artery show the highest collagen content as they are present throughout the entire stack. The laminar meshwork, which is barely visible in the prelaminar region, results in a markedly lower average collagen content. Within the lamina, higher collagen densities are found in the nasal and superior regions, whereas the inferior-temporal region is marked by considerably lower average collagen content.

This can be better appreciated by studying a three-dimensional rendering of the entire dataset. Using Amira, the whole stack was reconstructed in 3D as a Voltex object. By using OrthoSlice modules to scroll through the dataset along all three axes, the LC can be viewed from numerous angles. Rotating the reconstructed stack to the appropriate position allows for a longitudinal cross-section view that shows the expansion of the scleral canal and the posterior bowing of the LC (Fig. 7D).

Quantifying the dimensions of the ONH was achieved with MetaMorph's measuring tools. The diameter of the ellipsis-shaped scleral canal opening at the anterior (retinal) side was determined. For this eye, the ellipsis measured 1845 μm along the major and 1765 μm along the minor axis. The canal area expanded from 2.41 mm^2 at the most anterior aspect at Bruch's membrane, to 5.01 mm^2 at the posterior aspect of the dataset.

To obtain a quantitative analysis of collagen content and distribution throughout the entire ONH, 294 planes comprising the full dataset were analyzed individually for collagen density and scleral canal area. As the retinal ganglion cell axons pass through the pores formed by the collagen beams, the amount of space available

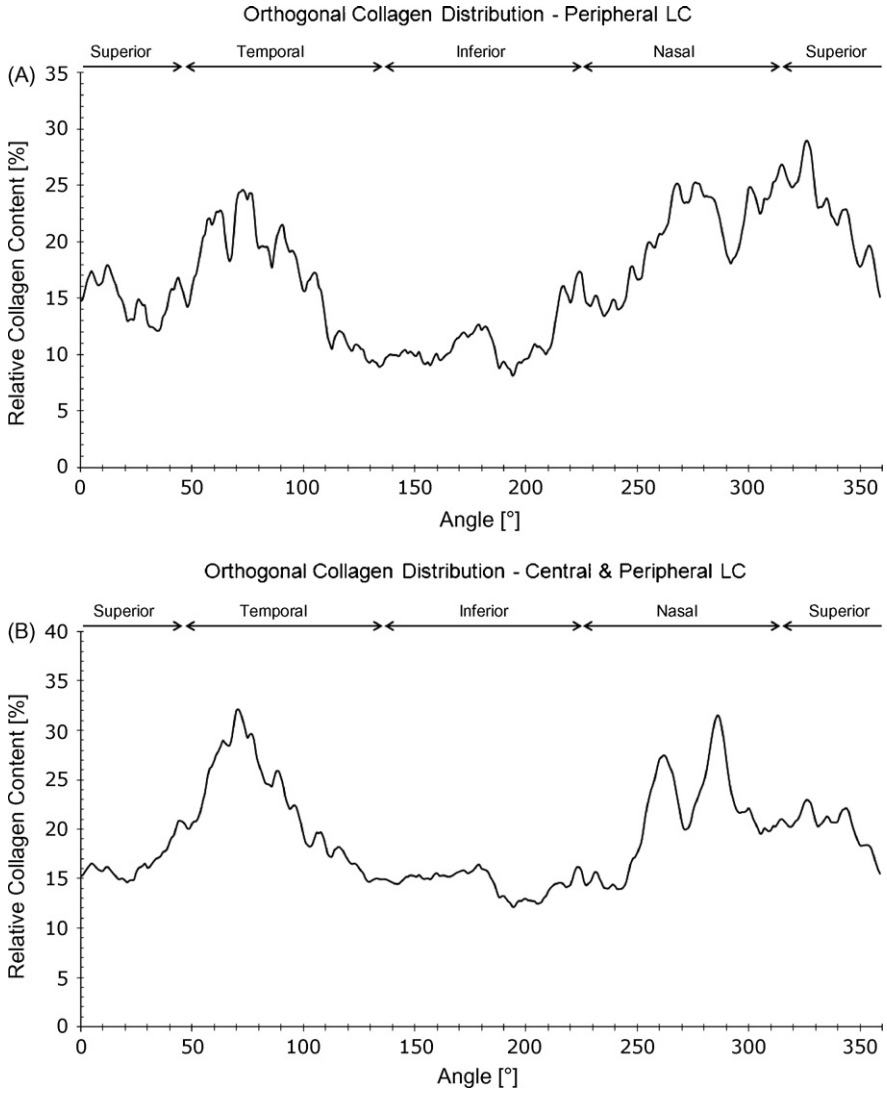

Fig. 8. Morphometric area analysis for collagen using line scans. The scan was performed twice: (A) shows the collagen content of the peripheral LC excluding the central portion containing the artery as shown in Fig. 1. (B) shows the collagen content of the entire LC. A running average over five data points was performed to smooth out the graphs while retaining information about relative positions. The central arterial walls are visible as twin local maxima in (B) at 260° and 285°.

to the axons is directly related to pore size. Fig. 7A shows an analysis of the prelaminar and laminar area. Here, the sclera canal widened posteriorly. Further, larger pore sizes dominated in the anterior portion of the lamina, but total pore area was restricted within the LC. Since the laminar meshwork was bowed in a posterior direction, the cross-sections of individual planes on the anterior side of the structure only contained collagen near the sclera canal wall. This coincided with an overall lower collagen content which increased as one moved down the canal in a posterior direction. The maximum collagen content was found in areas where the entire cross-section of the sclera canal was filled with collagen beams.

To better correlate the collagen distribution with clinical observations of the ONH, the dataset was divided into four anatomical regions as outlined in Fig. 1. Collagen density values were obtained by performing a plane-by-plane analysis of the entire LC. Analyzing the collagen content by anatomical region (Fig. 7B) reveals a steep increase in total collagen content about 140 μm into the stack, marking the beginning of the lamina. Within the lamina, the collagen content rises in all four sectors. However, the inferior quadrant showed a significantly lower average collagen content of $19.0 \pm 2.5\%$ throughout the laminar area compared to the other three quadrants which had collagen densities of $25.2 \pm 2.3\%$. This observation was consistent with the analyses presented in Figs. 4 and 5 as noted.

Based on data from Fig. 7, a plateau in relative collagen content in the laminar region is present within 60 planes or 120 μm starting approximately 400 μm from the surface of the stack. These planes were collapsed into a single plane by performing an average z projection after thresholding. The resulting image was then analyzed for relative collagen content by performing a radial analysis from the center of the image to the scleral canal wall through 360°. The scan was started at the 12 o' clock (superior) position and moved clockwise in single degree increments. For each line, the average collagen content was calculated. The resulting plots are shown in Fig. 8, demonstrating the lack of uniformity in the angular distribution of collagen density in the laminar region.

This scan was performed twice, with the first scan omitting the central portion of the lamina to exclude the central artery (Fig. 8A). The second scan includes data from both the central and peripheral LC (Fig. 8B). The high degree of variability in collagen content seen in this graph suggests a heterogeneous distribution of collagen in the LC. Collagen content varied significantly, even within each anatomical region.

4. Discussion

In this study, we successfully demonstrated a technique to generate high-resolution large-scale images of the Lamina Cribrosa in three dimensions by combining array tomography with second harmonic generation microscopy. A large body of research has been dedicated to producing accurate reconstructions of the ONH in three dimensions and to quantify those results in an attempt to better understand its structure and biomechanical properties [25,14,2,32,21,13,6,26,7]. The method demonstrated in this report addresses several major issues that researchers face when attempting to create these reconstructions by providing high resolution, a large field of view, and a highly specific signal.

High lateral resolution was achieved here by exploiting multiphoton effects for image generation rather than relying on conventional microscopy or digital imaging methods [32,6,7]. This allows for sub-micron resolution imaging of the ONH. In addition, as the SHG was exclusively due to the interaction of photons with collagen, the specificity of the signal matched that obtained with immunostaining and a monoclonal antibody.

The problems of significantly lower axial resolutions and associated issues such as shadowing, which are prevalent even in multiphoton or confocal microscopy, are addressed by using array tomography as described by Price et al. [23]. This approach generates consecutive thin slices, which are then imaged individually. Combining these two techniques allows us to create images with voxel resolutions of $0.91\ \mu m \times 0.91\ \mu m \times 2\ \mu m$. Higher resolutions are theoretically possible, but scanning time increases linearly with resolution.

Collecting several adjacent high-resolution images greatly expands our field of view to encompass the entire diameter of the ONH. The final result is an extremely detailed scan of the ONH including the prelaminar, laminar and postlaminar regions at higher resolutions than other optical methods.

Unlike EM or immunofluorescence microscopy, no staining or tissue digestion is necessary to isolate collagen. The emission of second harmonic light by collagen, as well as the lack of SHG in other structures in the ONH, provides a high degree of specificity of signal. The emission of SHG light from collagen has previously been exploited to analyze the lamina cribrosa [5] as well as the cornea [20]. Besides the SHG peak, there are several two photon excited fluorescent (TPEF) emission peaks in the spectrum of the ONH (Fig. 2) that contain additional structural information. Of particular interest is the distribution of elastin, which gives rise to a strong TPEF emission and is currently being investigated as part of a larger study.

With the ONH imaged as a series of high-resolution planes, various structural parameters such as the area and diameter of the scleral canal or the thickness of the LC can be determined precisely and efficiently. For this study, the basic dimensions of the scleral canal were easily obtained from the dataset. The axial lengths and areas correspond well to previously published values obtained by traditional means [26,15,4]. Based on the values we obtained and those in the literature, we can assume that any possible shrinkage of the tissue that occurred during the fixation, embedding or sectioning process was negligible.

Thresholding the image makes a quantitative analysis of ONH components possible. The data from the SHG channels allowed us to map both the overall relative collagen content as well as perform a detailed analysis of regional collagen density variations. Based on the collagen content, the total pore area can be calculated for each plane. The data showed a decrease in pore area inside the lamina (Fig. 7) which would limit the amount of space available for optic nerve axons. This restriction in available space may partially explain the known blockage of both retrograde and orthograde axoplasmic transport in the LC [18] that occurs with acute increases in IOP.

The quantitative density analysis indicates that the collagen meshwork that makes up the LC is non-uniform along all three axes in this 53-year-old male Hispanic eye. Collagen density varied both by geographic region and along the anterior–posterior axis. These areas of higher collagen density are more likely to resist changes in intraocular pressure when compared to lower density areas such as the collagen "hole" which is visible in the inferior temporal quadrant in Fig. 6. These same features are also visible in the radial analysis (Fig. 8). Peripherally, there are three broad density maxima. The two peaks at approximately 70° and 270° mark the presence of a dense band of collagen stretching across the lamina in nasal–temporal direction that is visible as a collagen "bridge" in Fig. 5. A local minimum at 40° suggests a thinning in the superior quadrant of the lamina that is also visible in Fig. 5. The aforementioned peaks remained visible when the central portion of the LC was included. Additionally, the central artery itself is now visible in the form of two distinct local maxima spaced approximately 15° apart marking the position of the arterial walls at 260° and 285°. As collagen beams appear to insert into the central artery, which in itself represents a dense collagenous structure, a biomechanical analysis of the LC should include the central artery, which is likely to provide additional stability.

While the biomechanical properties of the sclera are a function of several factors besides IOP, such as lateral and posterior boundary conditions, the non-uniform density of collagen in the lamina has interesting implications. If the LC were homogenous, one would expect a uniform distortion in a posterior direction as a response to an increase in IOP. That is, the pores in the central lamina would expand and move posteriorly, essentially sliding along the axons that pass through them and exerting comparatively little force. Nerve damage would most likely occur only in the peripheral regions where the pores would move laterally in addition to tilting posteriorly, as axons passing through the peripheral pores could be pinched by the tilting motion of the collagen beams.

However, this dataset indicates that collagen densities may vary significantly by geographic region. As a result, the effects of an increase in IOP may be far more complex. Areas of higher collagen density tend to resist pressure and distortion, while areas of low collagen density are displaced more easily. Notably, this holds true for the aforementioned "bridge" which appears to be further stabilized through the insertion of collagen beams into the central arterial wall and which is expected to experience comparatively little posterior displacement. Pores found in adjacent areas of lower collagen density should experience tilting as well as expansion posteriorly, similar to the pores found in the peripheral regions of the lamina close to the scleral canal wall as described in previous studies [5]. The tilting movement may exert particular stress on nerve axons, and since this stress is generated by relatively thin bands of collagen pressing against the axons, this could very well lead to axon damage and/or the interruption of blood flow as vessels are squeezed shut. The inferior temporal region has previously been identified as an area of greater susceptibility to nerve damage in early glaucoma [24]. This region in particular was marked by a lower overall collagen density (Figs. 6–8) and which is more likely to be susceptible to pressure changes.

While analyzing each plane as a separate two-dimensional picture provides important quantitative data, the complexity of the LC can better be appreciated by assembling the whole dataset as a single three-dimensional reconstruction. Creating a visual representation (Fig. 6) provides insight into to the three-dimensional organization of the LC. More importantly, with the availability of a 3D reconstruction it is possible to quantify the structure and dimensions of the ONH based on both an en face or orthogonal view as well as a longitudinal cross-section simultaneously by simply rotating the dataset to the appropriate angle. The 3D reconstruction also provides comprehensive data that is necessary to develop accurate finite element models of the LC in order to simulate elastic responses.

Additional studies will draw upon this method to include sectioning and scanning multiple eyes, generating a library of structural parameters based on race, gender, age and ocular health. To further supplement the datasets, the ONH could be scanned *ex vivo* before dissection under conditions of changing IOP to yield dynamic response data [5], which can then be combined with the structural information gained through array tomography.

With the use of a primate animal model of glaucoma, the reconstruction method described by Burgoyne et al. [6] makes it possible to follow the progression of glaucoma and to correlate reconstruction data with clinical observations, which is not possible with our human subject *ex vivo*-based approach. However, our method, which utilizes SHG, ensures a high degree of specificity of signal as well as superior axial and lateral resolutions. By adding *ex vivo* pre-scans of the intact eyes at variable pressures, dynamic response data can be added, which will allow us to correlate biomechanical responses with structural parameters.

A clinical application of this technique is conceivable, as structural information is derived from backwards-scattered SHG signals. By exploiting the optics of the eye, it may be possible to guide a short-pulsed beam onto the lamina cribrosa and collect the backscatter SHG signal to map the collagen structure *in vivo*, assuming that the power levels are below the safety threshold and that the pulse train does not experience excessive group velocity dispersion as it passes through the eye.

Conflict of interest

No conflict of interest.

Acknowledgements

The authors acknowledge NIH Grant EY16663 (JVJ), NIH Grant EY017959 (DJB), Research to Prevent Blindness, Discovery Fund for Eye Research, and Glaucoma Research Foundation (DJB).

References

[1] E. Abbe, Arch. f. mikroskop. Anat. 9 (1873) 413–468.
[2] A.J. Bellezza, C.J. Rintalan, H.W. Thompson, J.C. Downs, R.T. Hart, C.F. Burgoyne, Deformation of the lamina cribrosa and anterior scleral canal wall in early experimental glaucoma, Invest. Ophthalmol. Vis. Sci. 44 (2003) 623–637.
[3] M. Birch, D. Brotchie, N. Roberts, I. Grierson, The three-dimensional structure of the connective tissue in the lamina cribrosa of the human optic nerve head, Ophthalmologica 211 (1997) 183–191.
[4] R. Britton, S. Drance, M. Schulzer, G. Douglas, D. Mawson, The area of the neuroretinal rim of the optic nerve in normal eyes, Am. J. Ophthalmol. 103 (1987) 497–504.
[5] D. Brown, N. Morishige, A. Neekhra, D. Minckler, J. Jester, Application of second harmonic imaging microscopy to assess structural changes in optic nerve head structure ex vivo, J. Biomed. Opt. 12 (2007) 024029.
[6] C.F. Burgoyne, J.C. Downs, A.J. Bellezza, R.T. Hart, Three-dimensional reconstruction of normal and early glaucoma monkey optic nerve head connective tissues, Invest. Ophthalmol. Vis. Sci. 45 (2004) 4388–4399.
[7] J.C. Downs, H. Yang, C. Girkin, et al., Three-dimensional histomorphometry of the normal and early glaucomatous monkey optic nerve head: neural canal and subarachnoid space architecture, Invest. Ophthalmol. Vis. Sci. 48 (2007) 3195–3208.
[8] J. Ernest, A. Potts, Pathophysiology of the distal portion of the optic nerve. I. Tissue pressure relationships, Am. J. Ophthalmol. 66 (1968) 373–380.
[9] J. Ernest, A. Potts, Pathophysiology of the distal portion of the optic nerve. II. Vascular relationships, Am. J. Ophthalmol. 66 (1968) 380–387.
[10] A. Elkington, C. Inman, P. Steart, R. Weller, The structure of the lamina cribrosa of the human eye: an immunocytochemical and electron microscopical study, Eye (London 1987) 4 (1990) 42–57.
[11] D. Feitelson, The supercomputer industry in light of the Top500 data, Comput. Sci. Eng. (2005) 42–47.
[12] A. Fryczkowski, B. Grimson, R. Peiffer, Scanning electron microscopy of vascular casts of the human scleral lamina cribrosa, Int. Ophthalmol. 7 (1984) 95–100.
[13] M. Hernandez, X. Luo, F. Igoe, A. Neufeld, Extracellular matrix of the human lamina cribrosa, Am. J. Ophthalmol. 104 (1987) 567–576.
[14] M. Hernandez, W. Andrezejewska, A. Neufeld, Changes in the extracellular matrix of the human optic nerve head in primary open-angle glaucoma, Am. J. Ophthalmol. 109 (1990) 180–188.
[15] J. Jonas, G. Gusek, I. Guggenmoos-Holzmann, G. Naumann, Size of the optic nerve scleral canal and comparison with intravital determination of optic disc dimensions, Graefes Arch. Clin. Exp. Ophthalmol. 226 (1988) 213–215.
[16] J. Jonas, C. Mardin, U. Schlotzer-Schrehardt, G. Naumann, Morphometry of the human lamina cribrosa surface, Invest. Ophthalmol. Vis. Sci. 32 (1991) 401–405.
[17] K. Micheva, S. Smith, Array tomography: a new tool for imaging the molecular architecture and ultrastructure of neural circuits, Neuron 55 (2007) 25–36.
[18] D. Minckler, A. Bunt, I. Klock, Radioautographic and cytochemical ultrastructural studies of axoplasmic transport in the monkey optic nerve head, Invest. Ophthalmol. Vis. Sci. 17 (1978) 33–50.
[19] D. Minckler, G. Spaeth, Optic nerve damage in glaucoma, Surv. Ophthalmol. 26 (1981) 128–148.
[20] N. Morishige, A. Wahlert, M. Kenney, et al., Second-harmonic imaging microscopy of normal human and keratoconus cornea, Invest. Ophthalmol. Vis. Sci. 48 (2007) 1087–1094.
[21] J. Morrison, N. L'hernault, J. Jerdan, H. Quigley, Ultrastructural location of extracellular matrix components in the optic nerve head, Arch. Ophthalmol. 107 (1989) 123–129.
[22] M. Pease, S. Mckinnon, H. Quigley, L. Kerrigan-Baumrind, D. Zack, Obstructed axonal transport of BDNF and its receptor TrkB in experimental glaucoma, Invest. Ophthalmol. Vis. Sci. 41 (2000) 764–774.
[23] D. Price, S. Chow, N. Maclean, et al., High-resolution large-scale mosaic imaging using multiphoton microscopy to characterize transgenic mouse models of human neurological disorders, NeuroInformatics 4 (2006) 65–80.
[24] H. Quigley, E. Addicks, Regional differences in the structure of the lamina cribrosa and their relation to glaucomatous optic nerve damage, Arch. Ophthalmol. 99 (1981) 137–143.

[25] H. Quigley, R. Hohman, E. Addicks, R. Massof, W. Green, Morphologic changes in the lamina cribrosa correlated with neural loss in open-angle glaucoma, Am. J. Ophthalmol. 95 (1983) 673–691.
[26] H. Quigley, A. Brown, J. Morrison, S. Drance, The size and shape of the optic disc in normal human eyes, Arch. Ophthalmol. 108 (1990) 51–57.
[27] H. Quigley, S. Mckinnon, D. Zack, et al., Retrograde axonal transport of BDNF in retinal ganglion cells is blocked by acute IOP elevation in rats, Invest. Ophthalmol. Vis. Sci. 41 (2000) 3460–3466.
[28] S. Resnikoff, D. Pascolini, D. Etya'ale, et al., Global data on visual impairment in the year 2002, Bull. World Health Organ. 82 (2004) 844–851.
[29] S. Sawaguchi, B. Yue, T. Fukuchi, et al., Collagen fibrillar network in the optic nerve head of normal monkey eyes and monkey eyes with laser-induced glaucoma—a scanning electron microscopic study, Curr. Eye Res. 18 (1999) 143–149.
[30] A. Sadun, V. Carelli, S. Bose, F. Ross-Cisneros, P. Barboni, E. Ahrens, First application of extremely high-resolution magnetic resonance imaging to study microscopic features of normal and LHON human optic nerve, Ophthalmology 109 (2002) 1085–1091.
[31] D. Yan, F. Coloma, A. Metheetrairut, G. Trope, J. Heathcote, C. Ethier, Deformation of the lamina cribrosa by elevated intraocular pressure, BMJ (1994) 643–648.
[32] H. Yang, Jc. Downs, C. Girkin, et al., 3-D histomorphometry of the normal and early glaucomatous monkey optic nerve head: lamina cribrosa and peripapillary scleral position and thickness, Invest. Ophthalmol. Vis. Sci. 48 (2007) 4597–4607.